

A deep learning based reduced order modeling for stochastic underground flow problems

Yiran Wang*, Eric Chung[†] and Shubin Fu[‡]

November 29, 2021

Abstract

In this paper, we propose a deep learning based reduced order modeling method for stochastic underground flow problems in highly heterogeneous media. We aim to utilize supervised learning to build a reduced surrogate model from the stochastic parameter space that characterizes the possible highly heterogeneous media to the solution space of a stochastic flow problem to have fast online simulations. Dominant POD modes obtained from a well-designed spectral problem in a global snapshot space are used to represent the solution of the flow problem. Due to the small dimension of the solution, the complexity of the neural network is significantly reduced. We adopt the generalized multiscale finite element method (GMsFEM), in which a set of local multiscale basis functions that can capture the heterogeneity of the media and source information are constructed to efficiently generate globally defined snapshot space. Rigorous theoretical analyses are provided and extensive numerical experiments for linear and nonlinear stochastic flow are provided to verify the superior performance of the proposed method.

1 Introduction

Many subsurface flow problems are described as stochastic partial differential equations (SPDEs) [16, 20], in which the media properties are characterized by parameters. One often needs to solve the SPDEs for a large numbers of different realizations to obtain statistics of interested quantities. In data assimilation for estimating the permeability of the porous media [5], one also needs to run the forward model with different inputs. Besides, with the advancement of geostatistical modeling techniques, the characterization of media properties can be detailed at multiply scales. As a result, even a single simulation entails large demand of CPU and memory to get high-fidelity solutions, let alone running the models repeatedly. Moreover, obtaining highly accurate solutions is not necessary in certain scenarios [33]. All these motivate the development of reduced order modeling (ROM), in which the key idea is to utilize a significantly reduced low-dimensional model to replace the original full-order model with some sacrifice of accuracy for online evaluations.

The reduced basis (RB) method [20, 31] is an efficient and powerful reduced order modeling technique within the framework of offline-online simulations. The basis idea of this method is to extract a set of reduced bases from a collection of full-order snapshots to approximate the solutions in online evaluation stages so that one only needs to solve a very small-dimensional system. There are two popular approaches in the literature for extracting the reduced bases, one is the greedy algorithm [37, 32] and another one is the proper orthogonal decomposition (POD) [20, 25, 31]. The greedy algorithm aims to select an optimal basis set from the snapshot space with an error indicator,

*Department of Mathematics, The Chinese University of Hong Kong, Shatin, Hong Kong SAR.

[†]Department of Mathematics, The Chinese University of Hong Kong, Shatin, Hong Kong SAR.

[‡]Department of Mathematics, University of Wisconsin-Madison, WI, USA. Corresponding author (shubinfu89@gmail.com)

while the POD extracts the reduced bases utilizing the singular-value decomposition (SVD). Both methods has their advantages and disadvantages, we refer [4] for a systematical comparison. Once the reduced bases are available, one can employ the Galerkin projection of the full system to the RB space to get reduced-order solutions. The success of RB method relies on the decoupling between the offline and online stage [17] and which is often difficult or even impossible for a general nonlinear problem. The empirical interpolation method (EIM) [2] and its variants [28, 3] can help deal with this issue but may still suffer from inflexibility since they are problem-dependent and intrusive.

In this work, we consider the stochastic linear and nonlinear underground flow problems in highly heterogeneous porous media. We explore approximating the input-output mapping using artificial neural networks (ANNs), which can be traced back to neurophysiology [27]. Recently, ANNs have been utilized as an effective tool to solve high-dimensional partial differential equations in applied mathematics, biology, computational physics [7, 18, 19, 29]. In [21], the authors developed a non-intrusive RB method for parametrized partial differential equations. Our method also follow the offline-online framework as the RB method. In the offline stage, we first generate a number of high-fidelity global snapshots and then well-designed spectral problems motivated by rigorous analysis are solved in the global snapshot space to obtain a set of reduced bases. This spectral problem is similar to the SVD in POD, therefore we also denote this step as POD. Then we use these reduced bases to get some reduced solutions and therefore we can utilize the neural network to obtain a mapping from the parameter space to the reduced solution space. In the online stage, the well-trained neural network is adopted to evaluate the solutions with different inputs. The dimension of the output layer equals the dimension of the RB space and therefore this NN is light-weighted and easy to train.

Although the this reduced NN is easy to train, generating the data for training the NN is nontrivial since we have to solve the flow equations with traditional methods like the finite element or finite difference. As we have mentioned before, the porous media properties often vary several orders of magnitude and one needs to use very fine mesh to describe these properties, which will inevitably lead to huge dimension linear systems to be solved. Therefore, it is quite necessary to apply some local model reduction techniques for creating the snapshots efficiently.

Typically there are two types of local model reduction techniques, one is the homogenization [41, 13] and another one is the multiscale method, which includes many variants such as multiscale finite element methods [22, 6], multiscale mortar methods [1, 40], variational multiscale methods [23], and multiscale finite volume methods [12, 26]. Among these methods the multiscale finite element method (MsFEM) and its extension, the generalized multiscale finite element method (GMsFEM), have shown impressive performance for various types of heterogeneous problems [11, 10, 14, 36, 35, 39]. The basis idea of the GMsFEM is using a representative permeability field to generate a set of multiscale basis functions that include the media's heterogeneity information so that one can solve the problems in a relatively coarse grid. In [38], a local-global reduced order modeling method based on the GMsFEM and POD are proposed for stochastic underground flow in highly heterogeneous porous media. The combination is denoted by GMsFEM-POD method. Rigorous analysis and extensive numerical results show the impressive performance of this GMsFEM-POD for stochastic flow.

Here, we take advantage of the GMsFEM-POD method and the neural network and develop a combined method. The GMsFEM here serves to create the global snapshot space and the POD is utilized to get the RB and further generate the data for training the Neural network. We also explore the case that the source function used in generating the POD bases in offline stage is different with the source function used in online stage, which is not studied in [38]. Rich numerical examples are provided to show the performance of the proposed method. In particular, we study the influence of the number of local basis functions, the depth and width the NN on the accuracy of the method. We also compare the accuracy and efficiency of NN with the GMsFEM-POD [38] for the online valuation. Comparison of using different inputs are also investigated. Our proposed method is demonstrated to have good generalization power and high efficiency.

The paper is organized as follows. In Section 2, we review the Karhunen-Loève expansion

for characterizing the property of the porous media. GMsFEM-POD for generating the global reduced basis is described in Section 3, which contains the introduction of GMsFEM, POD and the convergence analysis of GMsFEM-POD. GMsFEM-POD based reduced neural network is presented in Section 4. Numerical simulations are shown in Section 5. We conclude the paper in Section 6.

2 Karhunen-Loève expansion

In this section, we briefly review the Karhunen-Loève (KL) expansion [15, 30] for characterizing the stochastic media properties. Similar to the Fourier series expansion, it aims to provide a representation of a random process using linear combination of a set of orthogonal bases. Let $(\Omega_r, \mathcal{F}, \mathcal{P})$ be a probability space. $\kappa(\mathbf{x}, \omega)$ is a random process defined in a compact spatial domain Ω and we have $\kappa(\mathbf{x}, \omega) \in L^2(\Omega \times \Omega_r)$.

We first define the inner product and norm as,

$$\begin{aligned} \langle p, q \rangle &= \int_{\Omega} pq, \quad \|p\|^2 = \int_{\Omega} |p|^2, \quad p, q \in L^2(\Omega), \\ \mathcal{A}_{\omega}(p, q) &= \int_{\Omega} \kappa(\mathbf{x}, \omega) \nabla p \cdot \nabla q, \quad \|p\|_{\omega}^2 = \mathcal{A}_{\omega}(p, p), \quad p, q \in H_{\kappa}(\Omega), \end{aligned}$$

where $H_{\kappa}(\Omega)$ is defined by

$$H_{\kappa}(\Omega) = \{p \mid \int_{\Omega} \kappa |\nabla p|^2 < \infty\}.$$

Suppose one has obtained a set of realizations $\{\kappa(\mathbf{x}, \omega_i)\}_{i=1}^{N_k}$. The covariance kernel $C(\mathbf{x}, \mathbf{y})$ is defined as follows,

$$C(\mathbf{x}, \mathbf{y}) = \mathbb{E}[(\kappa(\mathbf{x}, \omega) - \bar{\kappa}(\mathbf{x}))(\kappa(\mathbf{y}, \omega) - \bar{\kappa}(\mathbf{y}))],$$

where $\bar{\kappa}(\mathbf{x}) = \mathbb{E}[\kappa(\mathbf{x}, \omega)]$. We further generate a set of eigenvalues paired with eigenfunctions $\{\eta_i, \phi_i\}$ by using

$$\int_{\Omega} C(\mathbf{x}, \mathbf{y}) \phi(\mathbf{y}) = \eta \phi(\mathbf{x}). \quad (1)$$

Solving (1), one can obtain $\{\eta_i, \phi_i\}_{i=1}^{\infty}$. Without loss of generality, suppose $\{\eta_i\}$ is arranged in a decreasing order. Besides, $\{\phi_i(\mathbf{x})\}$ is normalized in the L^2 sense.

Then, we derive the KL expansion. For a specific sample permeability field $\kappa(\mathbf{x}, \omega)$, it can be expressed as:

$$\kappa(\mathbf{x}, \omega) = \bar{\kappa}(\mathbf{x}) + \sum_{i=1}^{\infty} \sqrt{\eta_i} p_i(\omega) \phi_i(\mathbf{x}), \quad (2)$$

where $p_i(\omega)$ is computed through

$$q_i(\omega) = \frac{1}{\sqrt{\eta_i}} \langle \kappa(\mathbf{x}, \omega) - \bar{\kappa}(\mathbf{x}), \phi_i(\mathbf{x}) \rangle.$$

We remark that $\{\eta_i\}$ are positive by the construction of $C(\mathbf{x}, \mathbf{y})$. We now are able to approximate any realization $\kappa(\mathbf{x}, \omega)$ using the truncated KL expansion as

$$\kappa(\mathbf{x}, \omega) \approx \bar{\kappa}(\mathbf{x}) + \sum_{i=1}^l \sqrt{\eta_i} p_i(\omega) \phi_i(\mathbf{x}). \quad (3)$$

Here, eigenfunctions corresponding to the l largest eigenvalues are chosen, which is determined by the error bound. In particular, once given a tolerance τ , we select the smallest l such that

$$\frac{\sum_{i=1}^l \eta_i}{\sum_{i=1}^{\infty} \eta_i} \geq \tau.$$

3 GMsFEM-POD

In this section, we present the local-global model reduction technique (GMsFEM-POD) for the stochastic linear flow problems.

3.1 Preliminaries

We consider the following underground flow problem [5]:

$$\begin{cases} S \frac{\partial p}{\partial t} - \operatorname{div}(\kappa(\mathbf{x}, \omega) \nabla p) = f(t, \mathbf{x}), & (t, \mathbf{x}, \omega) \in (0, T) \times \Omega \times \Omega_r, \\ p(t, \mathbf{x}) = 0, & (t, \mathbf{x}) \in (0, T) \times \partial\Omega, \\ p(0, \mathbf{x}) = g(\mathbf{x}), & (t, \mathbf{x}) \in \{t = 0\} \times \Omega. \end{cases} \quad (4)$$

Here, $\Omega \in \mathbb{R}^2$ is a compact spatial domain and Ω_r is the sample space. S is the specific storage which is assumed to be 1 in subsequent presentation for simplicity, $f(t, \mathbf{x})$ and $g(\mathbf{x})$ are given source term and initial function. T is the final simulation time instant. $\kappa(\mathbf{x}, \omega)$ is a random permeability field, without ambiguity, we use $\kappa := \kappa(\mathbf{x}, \omega)$. In particular, it is a high-contrast and heterogeneous permeability field with randomness. $p := p(t, \mathbf{x}; \omega)$ is defined to be the pressure, which is the solution of (4). We use the usual notations in Sobolev space such as $H_0^1(\Omega)$.

The variational formulation for the problem (4) is to find $p(t, \mathbf{x}; \omega) \in H_0^1(\Omega)$, where ω fixed, such that

$$\left\langle \frac{\partial p}{\partial t}, q \right\rangle + \mathcal{A}_\omega(p, q) = \langle f, q \rangle, \quad \forall q \in H_0^1(\Omega), \quad (5)$$

where $\mathcal{A}_\omega(p, q) = \int_\Omega \kappa(\mathbf{x}, \omega) \nabla p \cdot \nabla q$.

Backward Euler method is used to discretize (5) with time step $\Delta t > 0$, then we have

$$\left\langle \frac{p^{(n)} - p^{(n-1)}}{\Delta t}, q \right\rangle + \mathcal{A}_\omega(p^{(n)}, q) = \langle f^{(n)}, q \rangle, \quad \forall q \in H_0^1(\Omega), \quad (6)$$

where $p^{(n)} := p(t_n, \mathbf{x}; \omega)$ and $f^{(n)} = f(t_n, \mathbf{x})$. We then introduce the GMsFEM for (6).

3.2 GMsFEM

The key idea of the GMsFEM is to solve (4) in a relative coarse-mesh that may contains the variation of κ with carefully constructed multiscale basis. The construction of multiscale space consists of two stages: offline multiscale space and residual driven basis enrichment. We denote these two processes by offline stage 1 and offline stage 2. For the first stage, a initial multiscale space that only include local media information is constructed. It contains two steps: firstly, a local snapshot space is constructed; secondly, a set of well-designed local spectral problems are solved to reduce the dimension of the local snapshot space. In particular, only the eigenvectors corresponding to some smallest eigenvalues are used to construct the multiscale space. In offline stage 2, some residual-driven bases are iteratively constructed and incorporated into the previous offline multiscale space.

To better present the details of the GMsFEM, we denote \mathcal{T}_h be the fine-scale partition of Ω with h to be the fine mesh size. Let \mathcal{T}_H be a conforming partition of Ω with a set of coarse nodes

$\{\mathcal{N}_i\}_{i=1}^{N_c}$. H is defined to be the coarse mesh size. Define N_f, N_c to be the numbers of fine nodes and coarse nodes in \mathcal{T}_h and \mathcal{T}_H respectively. $N_{in,f}$ and $N_{in,c}$ are defined to be the number of inner fine and coarse nodes. Besides, let D_i be a coarse neighborhood corresponding to the coarse node \mathcal{N}_i , in particular, $D_i = \cup\{K \in \mathcal{T}_H, \mathcal{N}_i \in \bar{K}\}$. Figure 1 is an illustration of the notations. Each coarse neighborhood consists of four coarse blocks with a common coarse node. Moreover, $\forall K \in \mathcal{T}_H$, K are composed by some fine-scale blocks in \mathcal{T}_h . Let Q_{ms} be the standard finite element space

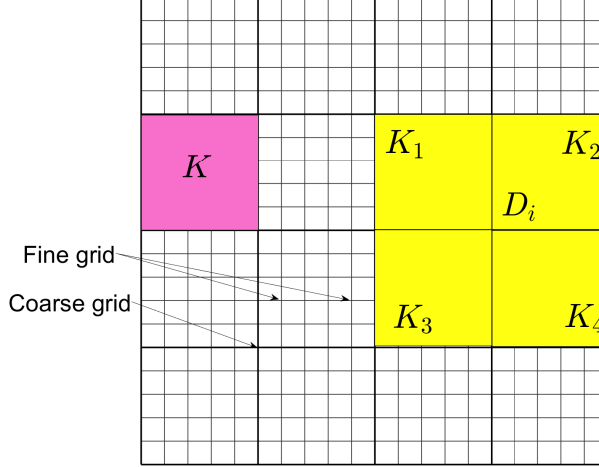


Figure 1: Illustration of mesh grids and coarse neighborhoods. A coarse neighborhood is composed of four elements sharing a common coarse grid.

which is composed of piecewise bilinear functions, $\gamma_1, \dots, \gamma_{N_{in,f}}$, corresponding to inner fine grids. In particular, $Q_{ms} = \text{span}\{\gamma_1, \dots, \gamma_{N_{in,f}}\}$. We further define $Q_{ms}^0 = \{q \in Q_{ms}; q = 0 \text{ on } \partial\Omega\}$, then fine-grid solution defined in Q_{ms}^0 can be obtained by solving the following equation:

$$\left\langle \frac{p_h^{(n)}}{\Delta t}, Q_{ms} \right\rangle + \mathcal{A}_\omega(p_h^{(n)}, Q_{ms}) = \left\langle \frac{p_h^{(n-1)}}{\Delta t} + f^{(n)}, Q_{ms} \right\rangle, \quad \forall Q_{ms} \in Q_{ms}^0, \quad (7)$$

$$\left\langle p_h^{(0)}, Q_{ms} \right\rangle = \langle g_h, Q_{ms} \rangle. \quad (8)$$

where g_h is L^2 project of g in Q_{ms}^0 .

For each coarse neighborhood D_i , let $J_h(D_i)$ be the set of the fine nodes of \mathcal{T}_h lying on ∂D_i , whose cardinality is denoted by $L_i \in \mathbb{N}^+$, i.e. $J_h(D_i) = \{x_j \in \partial D_i\}_{j=1}^{L_i}$. For each node $x_j \in \partial D_i$, a corresponding function δ_h^j is defined by

$$\delta_h^j(x_k) = \delta_{j,k} = \begin{cases} 1, & j = k, \\ 0, & j \neq k. \end{cases} \quad (9)$$

For each $j = 1, \dots, L_i$, the local snapshot function $\psi_j^{(i)}$ is the solution of following system,

$$\begin{aligned} -\text{div}(\kappa \nabla \psi_j^{(i)}) &= 0 \text{ in } D_i, \\ \psi_j^{(i)} &= \delta_h^j \text{ on } \partial D_i. \end{aligned} \quad (10)$$

Then, the local snapshot space corresponding to D_i is defined by $Q_{\text{snap}}^{(i)} := \text{span}\{\psi_j^{(i)} : j = 1, \dots, L_i\}$. The snapshot space is defined by $Q_{\text{snap}} := \bigoplus_{i=1}^{N_{\text{in},c}} Q_{\text{snap}}^{(i)}$.

Next, we perform the dimension reduction. For each $i = 1, \dots, N_{\text{in},c}$, the following spectral problem is solved,

$$\int_{D_i} \kappa \nabla z_j^{(i)} \cdot \nabla v = \lambda_j^{(i)} \int_{D_i} \hat{\kappa} z_j^{(i)} v \quad \forall v \in Q_{\text{snap}}^{(i)}, \quad j = 1, \dots, L_i, \quad (11)$$

where $\hat{\kappa} = \kappa \sum_{i=1}^{N_{\text{in},c}} |\chi_i|^2$. $\{\chi_i\}$ is a set of partition of unity functions. In particular, χ_i is supported in D_i and is the solution of the following equation

$$\begin{aligned} -\text{div}(\nabla \chi_i) &= 0 & \text{in } K_i \in \mathcal{T}_H, \\ \chi_i &= p_i & \text{on } \partial K_i. \end{aligned}$$

where p_i is linear function on \mathcal{T}_H . Without loss of generality, we sort the eigenvalues obtained in (11) in an increasing order, i.e., $\lambda_1^{(i)} \leq \dots \leq \lambda_{L_i}^{(i)}$. We define the multiscale space $Q_{\text{off}}^{(i)} := \text{span}\{\chi_i z_1^{(i)}, \dots, \chi_i z_{l_i}^{(i)}\}$, where $l_i \ll L_i$. In other words, only the modes associated with some smallest eigenvalues will be taken in the multiscale space. Moreover, define Λ to be the smallest eigenvalue whose corresponding eigenfunction is not included into the multiscale space.

$$\Lambda = \min_{1 \leq i \leq N_{\text{in},c}} \lambda_{l_i+1}^{(i)}. \quad (12)$$

The offline multiscale space is defined by $Q_{\text{off}} := \bigoplus_{i=1}^{N_{\text{in},c}} Q_{\text{off}}^{(i)}$. The multiscale solution p_H^n at $t = t_n$ is sought in Q_{off} by solving

$$\begin{aligned} \frac{1}{\Delta t} \langle p_H^n, v \rangle + \mathcal{A}_\omega(p_H^n, v) &= \left\langle \frac{1}{\Delta t} p_H^{n-1} + f^n, v \right\rangle, \\ \langle p_H^0, v \rangle &= \langle g, v \rangle, \quad \forall v \in Q_{\text{off}}. \end{aligned} \quad (13)$$

A residual driven bases enrichment technique can be adopted. Generally, there are two ways to add residual-driven bases. The first approach is to uniformly add the same number of bases in each local neighborhoods while the second one is to adaptively enrich the previous multiscale space. More specifically, only the the local multiscale space corresponding to large residual will be further enriched. In a time-marching process, residual-driven bases are constructed at different time steps, which leads to two different types of adaptive methods denoted by adaptive method A and adaptive method B. As for adaptive method A, every enrichment will be conducted from the offline multiscale space, which means the residual-driven bases generated from previous time steps will not be further used. On the other hand, the adaptive method B accumulates the residual-driven bases from previous time steps. Table 1 presents the flow of the above two methods.

Suppose the basis enrichment is performed at only at time t_n . Then the construction of multiscale space is shown as below:

1. Obtain the multiscale space Q_{off} in the offline stage 1.
2. At time t_n , compute the local residuals defined in (14).
3. Construct residual-driven bases in the local neighborhoods with largest local residuals.
4. Add residual-driven bases to Q_{off} to obtain Q_{ms} .

Note that residual-driven bases are only constructed once, which means adaptive method A and B are the same here. In [9], a rigorous analysis in terms of the residual-driven bases construction is given. We here present the adaptive method in detail. Let $p_H^n \in Q_{\text{ms}}$ be the solution to (13)

at $t = t_n$. Fixed a coarse neighborhood D_i , let $Q_i = H_0^1(D_i) \cap Q_{\text{snap}}$ equipped with the norm $\|p\|_\omega^2 := \int_{D_i} \kappa |\nabla p|^2$. We further define the local residual operator $\mathcal{R}_i^n : Q_i \rightarrow \mathbb{R}$ by

$$\mathcal{R}_i^n(q; p_H^n) := \int_{D_i} \left(\frac{1}{\Delta t} p_H^{n-1} + f^n \right) q - \int_{D_i} \left(\kappa \nabla p_H^n \cdot \nabla q + \frac{1}{\Delta t} p_H^n q \right), \quad \forall q \in Q_i. \quad (14)$$

A global residual operator $\mathcal{R}^n : Q_{\text{snap}} \rightarrow \mathbb{R}$ is defined by

$$\mathcal{R}^n(q; p_H^n) := \int_\Omega \left(\frac{1}{\Delta t} p_H^{n-1} + f^n \right) q - \int_\Omega \left(\kappa \nabla p_H^n \cdot \nabla q + \frac{1}{\Delta t} p_H^n q \right), \quad \forall q \in Q_{\text{snap}}. \quad (15)$$

We use $\|\mathcal{R}_i^n\|_O$, $\|\mathcal{R}^n\|_O$ to denote the operator norm of \mathcal{R}_i^n and \mathcal{R}^n , respectively. Let $R_i^n := \|\mathcal{R}_i^n\|_O$ and $R^n := \|\mathcal{R}^n\|_O$. A residual-driven basis $\phi_i \in Q_i$ are obtained by solving

$$\mathcal{A}_\omega(\phi_i, q) = \mathcal{R}_i^n(q; p_H^n), \quad \forall q \in Q_i. \quad (16)$$

Let k be the level of the enrichment and $Q_{\text{ms}}^{(n),k}$ be the multiscale space after k enrichment iterations at time t_n . $p_H^{(n),k}$ is defined to be the multiscale solution sought in $Q_{\text{ms}}^{(n),k}$. Suppose $\mathcal{I} \subset \{1, 2, \dots, N_{\text{in},c}\}$ is the index set over some non-overlapping coarse neighborhoods, where the previous multiscale space is enriched. In particular, for each $i \in \mathcal{I}$, a residual-driven basis ϕ_i is attained by solving (16). We further define $Q_{\text{ms}}^{(n),k+1} := Q_{\text{ms}}^{(n),k} \oplus \text{span}\{\phi_i : i \in \mathcal{I}\}$. We summarize the adaptive enrichment method in Table 1.

Prepare: $Q_{\text{off}}, \theta \in [0, 1], \tau > 0$.

On a specific time step t_n ,

let $Q_{\text{ms}}^{(n),0} = Q_{\text{off}}$ (method A) or $Q_{\text{ms}}^{(n),0} = Q_{\text{ms}}^{(n-1)}$ (method B).

for the k -th enrichment

Input: $Q_{\text{ms}}^{(n),k-1}$.

1. Obtain the multiscale solution $p_H^{(n),k}$ by solving the reduced system (13) in $Q_{\text{ms}}^{(n),k-1}$.

Compute the global residual $\|\mathcal{R}^n\|_O$ and break the for loop if $\|\mathcal{R}^n\|_O \leq \tau$.

2. Select a set of nonoverlapping coarse neighborhoods where basis enrichment is needed.

Compute the local residuals $R_1^n, \dots, R_{N_{\text{in}}}^n$ (defined in (14)).

Find $R_{k_1}^n, \dots, R_{k_m}^n$ (the biggest m local residuals) such that $R_{k_1}^n + \dots + R_{k_m}^n \geq \theta R^n$.

3. Solve the residual-driven bases and perform the basis enrichment.

Solve (16) in the above m local domains with above residuals $R_{k_1}^n, \dots, R_{k_m}^n$

respectively to obtain $\phi_{k_1}^{(n),k}, \dots, \phi_{k_m}^{(n),k}$.

$Q_{\text{ms}}^{(n),k} = Q_{\text{ms}}^{(n),k-1} \oplus \text{span}\{\phi_{k_1}^{(n),k}, \dots, \phi_{k_m}^{(n),k}\}$.

Output: $Q_{\text{ms}}^{(n),k}$.

end for

Table 1: Adaptive enrichment methods.

3.3 Proper orthogonal decomposition

In [38], a specific form of proper orthogonal decomposition (POD) is proposed, which is motivated by the analysis. In this part, we briefly review the main steps. Similar to the construction of an offline local multiscale space, the first step to to generate snapshot space. However, the local snapshot functions(10) are solved in local neighborhoods, the snapshot space here denoted by \mathcal{S} is spanned by a set of global snapshot functions whose supports are the global domain Ω . When \mathcal{S} is constructed, a spectral decomposition is performed to reduce the dimension.

First of all, we introduce some notations. We define $p_H^{(i)}(\mathbf{x}; \tilde{\omega}, \tilde{f})$ to be the solution to (13) at $t = t_i$ associated with $\kappa(\mathbf{x}, \tilde{\omega})$ and source term \tilde{f} . Note that $\tilde{\omega}$ and \tilde{f} are fixed. Suppose one has obtained a set of multiscale solutions $\{p_H^{(i)}(\mathbf{x}; \tilde{\omega}, \tilde{f})\} \subset Q_{\text{ms}}$. Let $\Delta p_H^{(i)}$ be a finite difference operator in time, i.e., $\Delta p_H^{(i)} = \frac{p_H^{(i)} - p_H^{(i-1)}}{\Delta t}$, for $1 \leq i \leq n$. We further define $\mathcal{S} := \{p_H^{(i)}(\mathbf{x}; \tilde{\omega}, \tilde{f}), \Delta p_H^{(i)}(\mathbf{x}; \tilde{\omega}, \tilde{f})\}_{i=1}^n$. Without ambiguity, we also denote $p_H^{(i)} = p_H^{(i)}(\mathbf{x}; \tilde{\omega}, \tilde{f})$ for simplicity. Then we solve following spectral problem:

$$\sum_{i=1}^n \mathcal{A}_{\tilde{\omega}}(p_H^{(i)}, u) p_H^{(i)} + W^2 \sum_{i=1}^n \mathcal{A}_{\tilde{\omega}}(\Delta p_H^{(i)}, u) \Delta p_H^{(i)} = \lambda u. \quad (17)$$

Here W is selected such that

$$\|p\|^2 \leq W \|p\|_{\tilde{\omega}}^2, \quad \forall p \in H_0^1(\Omega), \quad (18)$$

which is derived from Poincaré inequality. Hence a set of eigenvalues paired with eigenfunctions $\{\lambda_i, u_i\}$ are obtained. $\{\lambda_i\}$ are sorted in a decreasing order. $\{u_i\}$ are normalized such that $\mathcal{A}_{\tilde{\omega}}(u_i, u_j) = \delta_{ij}$. We take l eigenfunctions corresponding to l biggest eigenvalues. We denote the final reduced space by $Q_{l, \mathcal{S}}$.

Finally, we give a complete version of the GMsFEM-POD. The method contains three main steps:

1. Generate the multiscale space Q_{ms} associated with a representative permeability field $\kappa(\tilde{\omega})$;
2. Use Q_{ms} to obtain a global snapshot space \mathcal{S} ;
3. Perform POD on \mathcal{S} to get the final POD space $Q_{l, \mathcal{S}}$.

More specifically, first of all, with Theorem 3, we choose a representative permeability field $\kappa(\tilde{\omega})$, based on which one can construct a multiscale space Q_{ms} . We remark that one adaptive enrichment method (see Table 1) is applied to generate residual-driven bases. Secondly, based on the prepared Q_{ms} , one can solve a set of multiscale solutions $\{p_H^{(i)}\}_{i=1}^n$, which are projected back to the fine grid \mathcal{T}_h . With $\{p_H^{(i)}\}_{i=1}^n$ one can generate $\{\Delta p_H^{(i)}\}_{i=1}^n$ and further get the snapshot space \mathcal{S} . Using the spectral problem (17), one can obtain a set of eigenfunctions $\{u_i\}_{i=1}^l$ corresponding to l largest eigenvalues $\{\lambda_i\}_{i=1}^l$. Then $Q_{l, \mathcal{S}}$ is spanned using $\{u_i\}_{i=1}^l$.

3.4 Convergence analysis

In this subsection, we prove the convergence of the proposed method. First of all, we denote $p_h^{(n)}(\mathbf{x}; \omega, f)$, $p_H^{(n)}(\mathbf{x}; \omega, f)$ and $q_l^{(n)}(\mathbf{x}; \omega, f)$ to be the fine solution, multiscale solution and POD solution corresponding to $\kappa(\mathbf{x}, \omega)$ and source f . In particular, we have

$$\begin{aligned} \frac{1}{\Delta t} \langle p_h^{(n)}, v \rangle + \langle \kappa(\mathbf{x}, \omega) \nabla p_h^{(n)}, \nabla v \rangle &= \left\langle \frac{1}{\Delta t} p_h^{(n-1)} + f^n, v \right\rangle, \\ \langle p_h^{(0)}, v \rangle &= \langle g, v \rangle, \quad \forall v \in Q_h^0. \end{aligned} \quad (19)$$

$$\begin{aligned} \frac{1}{\Delta t} \langle p_H^{(n)}, v \rangle + \langle \kappa(\mathbf{x}, \omega) \nabla p_H^{(n)}, \nabla v \rangle &= \left\langle \frac{1}{\Delta t} p_H^{(n-1)} + f^n, v \right\rangle, \\ \langle p_H^{(0)}, v \rangle &= \langle g, v \rangle, \quad \forall v \in Q_{\text{ms}}. \end{aligned} \quad (20)$$

$$\begin{aligned} \frac{1}{\Delta t} \langle q_l^{(n)}, v \rangle + \langle \kappa(\mathbf{x}, \omega) \nabla q_l^{(n)}, \nabla v \rangle &= \left\langle \frac{1}{\Delta t} q_l^{(n-1)} + f^n, v \right\rangle, \\ \langle q_l^{(0)}, v \rangle &= \langle g, v \rangle, \quad \forall v \in Q_{l, \mathcal{S}}. \end{aligned} \quad (21)$$

We aim at estimating the difference between $p_h^{(n)}$ and $q_l^{(n)}$. Since we construct the multiscale space based on a specific $\tilde{\omega}$ and \tilde{f} , which may be different with ω and f . In other words, the multiscale space constructed with $\tilde{\omega}$ and \tilde{f} will be used to solve the concerned equation corresponding to different ω and f in the online stage. We split the difference into six parts as follows.

$$\begin{aligned}
p_h^{(n)}(\mathbf{x}; \omega, f) - q_l^{(n)}(\mathbf{x}; \omega, f) &= p_h^{(n)}(\mathbf{x}; \omega, f) - p_h^{(n)}(\mathbf{x}; \tilde{\omega}, f) + p_h^{(n)}(\mathbf{x}; \tilde{\omega}, f) - p_h^{(n)}(\mathbf{x}; \tilde{\omega}, \tilde{f}) \\
&\quad + p_h^{(n)}(\mathbf{x}; \tilde{\omega}, \tilde{f}) - p_H^{(n)}(\mathbf{x}; \tilde{\omega}, \tilde{f}) + p_H^{(n)}(\mathbf{x}; \tilde{\omega}, \tilde{f}) - q_l^{(n)}(\mathbf{x}; \tilde{\omega}, \tilde{f}) \\
&\quad + q_l^{(n)}(\mathbf{x}; \tilde{\omega}, \tilde{f}) - q_l^{(n)}(\mathbf{x}; \tilde{\omega}, f) + q_l^{(n)}(\mathbf{x}; \tilde{\omega}, f) - q_l^{(n)}(\mathbf{x}; \omega, f) \\
e^{(n)} &:= e_1^{(n)} + e_2^{(n)} + e_3^{(n)} + e_4^{(n)} + e_5^{(n)} + e_6^{(n)}.
\end{aligned} \tag{22}$$

In particular, $e^{(n)}$ and $e_i^{(n)}$ ($i = 1, \dots, 6$) are defined by:

$$\begin{aligned}
e^{(n)} &= p_h^{(n)}(\mathbf{x}; \omega, f) - q_l^{(n)}(\mathbf{x}; \omega, f), \\
e_1^{(n)} &= p_h^{(n)}(\mathbf{x}; \omega, f) - p_h^{(n)}(\mathbf{x}; \tilde{\omega}, f), \\
e_2^{(n)} &= p_h^{(n)}(\mathbf{x}; \tilde{\omega}, f) - p_h^{(n)}(\mathbf{x}; \tilde{\omega}, \tilde{f}), \\
e_3^{(n)} &= p_h^{(n)}(\mathbf{x}; \tilde{\omega}, \tilde{f}) - p_H^{(n)}(\mathbf{x}; \tilde{\omega}, \tilde{f}), \\
e_4^{(n)} &= p_H^{(n)}(\mathbf{x}; \tilde{\omega}, \tilde{f}) - q_l^{(n)}(\mathbf{x}; \tilde{\omega}, \tilde{f}), \\
e_5^{(n)} &= q_l^{(n)}(\mathbf{x}; \tilde{\omega}, \tilde{f}) - q_l^{(n)}(\mathbf{x}; \tilde{\omega}, f), \\
e_6^{(n)} &= q_l^{(n)}(\mathbf{x}; \tilde{\omega}, f) - q_l^{(n)}(\mathbf{x}; \omega, f).
\end{aligned}$$

In [38], the total error was split into four parts. In this paper, we add $e_2^{(n)}$ and $e_5^{(n)}$ to denote the errors from source terms. In particular, we have the following theorem to give error bound for e_2 and e_5 . It suffices to estimate e_2 and the estimation for e_5 are almost the same.

Theorem 1. *Let $p_{h,1}^{(n)} := p_h^{(n)}(\mathbf{x}; \omega, f)$ and $p_{h,2}^{(n)} := p_h^{(n)}(\mathbf{x}; \omega, \tilde{f})$ be fine solutions to (19) corresponding to f and \tilde{f} . And $q_{l,1}^{(n)} := q_l^{(n)}(\mathbf{x}; \omega, f)$ and $q_{l,2}^{(n)} := q_l^{(n)}(\mathbf{x}; \omega, \tilde{f})$ are POD solutions to (21) corresponding to f and \tilde{f} . Then it holds that*

$$\|e_2^{(n)}\| \leq \Delta t \sum_{i=1}^n \|f^{(i)} - \tilde{f}^{(i)}\|. \tag{23}$$

$$\|e_5^{(n)}\| \leq \Delta t \sum_{i=1}^n \|f^{(i)} - \tilde{f}^{(i)}\|. \tag{24}$$

Proof. $\forall 1 \leq i \leq n$, $p_{h,1}^{(i)}$ and $p_{h,2}^{(i)}$ satisfy the following equations respectively,

$$\frac{1}{\Delta t} \langle p_{h,1}^{(i)}, v \rangle + \langle \kappa(\mathbf{x}, \omega) \nabla p_{h,1}^{(i)}, \nabla v \rangle = \left\langle \frac{1}{\Delta t} p_{h,1}^{(i-1)} + f^{(i)}, v \right\rangle. \tag{25}$$

$$\frac{1}{\Delta t} \langle p_{h,2}^{(i)}, v \rangle + \langle \kappa(\mathbf{x}, \omega) \nabla p_{h,2}^{(i)}, \nabla v \rangle = \left\langle \frac{1}{\Delta t} p_{h,2}^{(i-1)} + \tilde{f}^{(i)}, v \right\rangle. \tag{26}$$

Subtract (26) from (25) and we obtain

$$\frac{1}{\Delta t} \langle e_2^{(i)}, v \rangle + \langle \kappa(\mathbf{x}, \omega) \nabla e_2^{(i)}, \nabla v \rangle = \left\langle \frac{1}{\Delta t} e_2^{(i-1)} + f^{(i)} - \tilde{f}^{(i)}, v \right\rangle. \tag{27}$$

Taking $v = e_2^{(i)}$ in (27) and applying Cauchy-Schwartz inequality, it holds that

$$\|e_2^{(i)}\|^2 + \Delta t \|e_2^{(i)}\|_\omega^2 \leq \|e_2^{(i-1)}\| \|e_2^{(i)}\| + \Delta t \|f^{(i)} - \tilde{f}^{(i)}\| \|e_2^{(i)}\|.$$

Hence we attain

$$\|e_2^{(i)}\| \leq \|e_2^{(i-1)}\| + \Delta t \|f^{(i)} - \tilde{f}^{(i)}\| \quad (28)$$

Adding (28) for $i = 1, \dots, n$, we conclude with

$$\|e_2^{(n)}\| \leq \|e_2^{(0)}\| + \Delta t \sum_{i=1}^n \|f^{(i)} - \tilde{f}^{(i)}\|.$$

Since $e_2^{(0)} = p_{h,1}^{(0)} - p_{h,2}^{(0)} = 0$, (23) has been attained. Same strategies hold for the estimation for $\|e_5\|$, then we have derive (24). \square

Before the main theorem, we define the elliptic projection.

Definition 2. We define $R_H : H_0^1(\Omega) \rightarrow Q_{ms}$ to be the elliptic projection with respect to the energy inner product, therefore, we have

$$\langle \kappa \nabla (R_H p - p), \nabla q \rangle = 0, \quad \forall q \in Q_{ms}.$$

We now consider other error components in (22), which the same strategy is applied as that in [38]. And we combine the Theorem 4 in [38] with the Theorem 1 in this paper to derive the final result.

Theorem 3. Almost nearly for all $\omega \in \Omega_r$, $p_h^{(n)}$ and $q_l^{(n)}$ are the solutions to (19) and (21) corresponding to ω and f then there exists a corresponding $\tilde{\omega}$ such that

$$\begin{aligned} \|p_h^n - q_l^n\|^2 &\leq C \left(\|p_h^0 - p_H^0\|^2 + \|p_h^0 - R_H u_h^0\|^2 + \sum_{i=1}^n (\gamma(H))^4 \kappa_{\min}(\tilde{\omega})^{-1} \|\kappa^{-\frac{1}{2}}(\tilde{f}^i - \partial_t p_h^i)\|^2 \right) \\ &+ C(\Delta t + Q) \sum_{p=l+1}^M \lambda_p + \frac{C\epsilon^2}{\kappa_{\min}(\omega)\kappa_{\min}(\tilde{\omega})} + \Delta t \sum_{i=1}^n \|f^{(i)} - \tilde{f}^{(i)}\|, \end{aligned} \quad (29)$$

where $\tilde{\omega}, \tilde{f}$ are used to construct the multiscale space. Moreover, $\gamma(H)$ is defined as below:

$$\gamma(H) = \sqrt{2C_{ov}H} \max_{i=1, \dots, N_{in}} \{C_0 H C_{poin}(D_i) + \sqrt{C_{poin}(D_i)}\} + C_1 \sqrt{20C_{ov}(H^2\Lambda)^{-\frac{1}{2}}}.$$

The concerned constants are defined as follows:

$$C_{poin}(D_i) := H^{-2} \max_{\eta \in H_\kappa(D_i)} \frac{\int_{D_i} \kappa \eta^2}{\int_{D_i} \kappa |\nabla \eta|^2}. \quad (30)$$

$$C_{poin}(\Omega) := \text{diam}(\Omega)^{-2} \max_{\eta \in H_\kappa(\Omega)} \frac{\int_{\Omega} \kappa \eta^2}{\int_{\Omega} \kappa |\nabla \eta|^2}. \quad (31)$$

$$C_{ov} := \max_{K \in \mathcal{T}^H} \#\{O_i : K \subset D_i \text{ for } i = 1, \dots, N_{in}\}. \quad (32)$$

Λ is defined in (12). The constants $C_{poin}(D_i)$ and $C_{poin}(\Omega)$ are independent of κ . C_0 depends on Ω , the size and shape of subsets P_j for $j = 1, \dots, s$, the space dimension d and the coefficient κ but it is independent of the distances between the inclusions P_k and P_j for $k, j = 1, \dots, s$. However, the precise dependence of the constant C_0 on κ is still unknown. The constant C_1 is given by $C_1 := H \max_{i=1, \dots, N_{in}} \{\sqrt{C_{poin}(D_i)}\} + 2\text{diam}(\Omega)\sqrt{C_{poin}(\Omega)}$.

4 A coupled GMsFEM-POD with Deep Learning

In this section, we introduce our GMsFEM-POD based neural network. First of all, we give some preliminaries of artificial neural networks (ANNs). Then, we will use GMsFEM-POD to construct a reduced-order neural network.

4.1 Neural Network

An ANN is designed to learn a map \mathcal{F} from existing data. In particular, let $\{x_i, y_i\}_{i=1}^N$ be the given data and N is the number of samples in the set then the data is generated using $\mathcal{F}(x_i) = y_i$, for $1 \leq i \leq N$. In order to predict $\mathcal{F}(x_i)$, for $i = N + 1, \dots, N + M$, we use ANN. Generally, an ANN is composed of a set of connected neurons, which are arranged in some layers, i.e. an input, an output layer, and some hidden layers. Each neuron in a hidden layer has some inputs and produces a single output. In particular, for a neuron in an intermediate layer, a bias is added to a weighted sum of inputs that come from the previous layer. The result is passed through an activation function σ to produce a single output to the subsequent layer. A neural network of D hidden layers is written in the following form:

$$\mathcal{N}(x; \theta) = \sigma(W_D \sigma(\dots \sigma(W_2 \sigma(W_1 x + b_1) + b_2) \dots) + b_D) \quad (33)$$

where W_i and b_i are the weight and bias in the i -th layer, for $1 \leq i \leq D$. $\theta := (W_1, \dots, W_D, b_1, \dots, b_D)$ and x is defined to be the input. σ is a specific activation function. Define y to be the output of the network. There are some common activation functions, such as Sigmoid (Logistic), Hyperbolic Tangent (Tanh), Rectified Linear Unit (ReLU), Leaky ReLU and Exponential Linear Units (ELU). We use ReLU in the work. The process of computing y from x is called forward propagation, whose mathematical description is shown in (33). The goal of training a NN is to find an optimal set of parameters θ^* such that

$$\theta^* = \underset{\theta}{\operatorname{argmin}} \mathcal{L}(\theta), \quad (34)$$

where \mathcal{L} is a cost function. Mean-squared error is a most commonly used metric equipped with the following loss function

$$\mathcal{L}(\theta) := \frac{1}{N} \sum_{i=1}^N \|y_i - \mathcal{N}(x_i; \theta)\|_2^2. \quad (35)$$

To solve (34), we need to use some optimization methods. There are many popular optimization methods applied in machine learning. Generally, they are divided into three categories: : first-order optimization methods, high-order optimization methods and heuristic derivative-free optimization methods [34]. Representative examples for the above three are stochastic gradient method, Newton's method and coordinate descent method, respectively. In this work, we use Adam optimization, which is an extension of stochastic gradient descent.

4.2 A reduced-order network

In this subsection, we present our GMsFEM-POD based neural network. With GMsFEM-POD, a set of POD bases $\{u_i\}_{i=1}^l$ is obtained. Define $U_j \in \mathbb{R}^{N_f}$ to be the fine-grid projection of u_j , i.e. $U_j[i] = u_j(\mathbf{x}_i)$, for $\mathbf{x}_i \in \mathcal{T}_h$ and $1 \leq j \leq l$ and further define $M_p := [U_1, \dots, U_l] \in \mathbb{R}^{N_f \times l}$. We solve (21) corresponding to a realization ω with the globally defined POD bases and denote the corresponding solution $\mathbf{c} \in \mathbb{R}^l$. In other words, \mathbf{c} is the coefficient vector of p with respect to $\{U_j\}_{j=1}^l$. Thus, if one solves (21) in a fixed POD space, it suffices to compute the coefficient vector \mathbf{c} . Hence, we define a mapping $\tilde{\mathcal{F}}$ from KL expansion coefficients and a specific time $t \in (0, T]$ to POD coefficients \mathbf{c} , i.e., $\tilde{\mathcal{F}} : (\mathbf{x}, t) \rightarrow \mathbf{c}$. And we utilize an ANN to approximate $\tilde{\mathcal{F}}$. The algorithm

Deep learning based GMsFEM-POD	
Step 1:	Obtain a set of POD basis $\{u_i\}_{i=1}^l$.
Step 2:	Solve(21) with $\{u_i\}_{i=1}^l$ to obtain \mathcal{D}_1 and \mathcal{D}_2 , where \mathcal{D}_1 is the training set and \mathcal{D}_2 is the test set.
Step 3:	Training process. k-fold cross-validation is applied to divide \mathcal{D}_1 into a training set and a test set.
Step 4:	Test process. Evaluate the performance of trained NN in \mathcal{D}_2 .

Table 2: A workflow of deep learning-based reduced order method, which combines deep learning and GMsFEM-POD.

is shown in the Table 2. Once the map $\tilde{\mathcal{F}}$ is constructed, one can obtain the solution of (4) at time T with tremendous boost speed for each realization of κ . We note that the fine-grid projection of reduced order solution spanned by the POD bases can also be obtained via $p = M_p \mathbf{c}$.

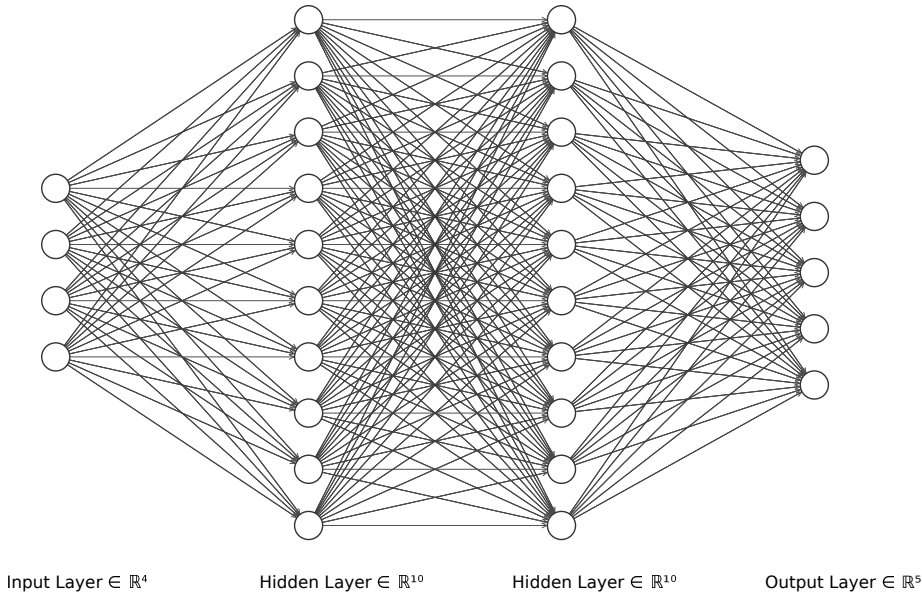


Figure 2: An illustration of a feedforward neural network. A network is composed of an input layer, two hidden layers and an output layer.

5 Numerical simulations

In this section, we test our method with linear and nonlinear stochastic flows. Two types of NNs are formulated: time-independent and time-dependent, where the difference lies in whether a specific time is included in the input. We first present general experiment settings in the subsection 5.1. In the next part, we investigate our method with linear stochastic flow. First of all, we compare NNs with different width and depth in subsection 5.2.1. With the NN architecture fixed, we compare the NN predictions with POD solutions in subsection 5.2.2. We show results from both time-independent and time-dependent NNs in subsections 5.2.1 and 5.2.2. Furthermore, we explore the influences from the numbers of KL expansion terms, POD bases and local multiscale bases on the performance of our method. Time-independent and time-dependent cases are considered separately in subsections 5.2.3 and 5.2.4. A nonlinear flow problem is explored in subsection 5.3,

in which effects of NN architectures are shown in subsection 5.3.1. Lastly, a comparison between NN predictions and POD solutions is shown in subsection 5.3.2.

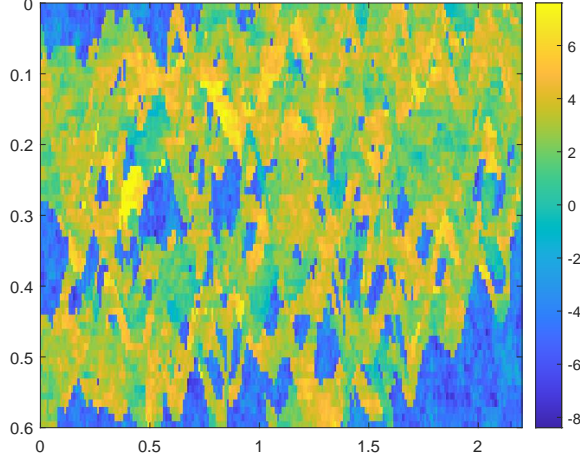


Figure 3: Display of the permeability field in natural logarithm scale.

5.1 Basic settings

We extract the last layer of the tenth SPE comparative solution project (SPE10 [8]) to serve as the mean permeability field $\bar{\kappa}(\mathbf{x})$, whose resolution is 220×60 and is shown in Figure 3. High heterogeneity of the media can be observed, which brings computational challenges in solving the concerned equations. Therefore, the media can be a good test for our multiscale method and it is indeed a benchmark model for assess some relevant numerical methods. We set the computation domain Ω to be $[0, 2.2] \times [0, 0.6]$ and the number of coarse-grid nodes to be 22×6 , therefore $h = 0.01$ and $H = 0.1$. For the KL expansion, the covariance function is defined as

$$C(\mathbf{x}, \mathbf{y}) = \sigma^2 \exp\left(-\frac{|x_1 - y_1|^2}{l_1^2} - \frac{|x_2 - y_2|^2}{l_2^2}\right), \quad (36)$$

where $\sigma^2 = 2$, $l_1 = l_2 = 0.5$.

5.2 Linear flow

Training data and test data are obtained with source terms f_1 and f_2 , respectively. Specifically, $\forall t \in [0, T]$, and $\mathbf{x} \in \Omega$,

$$f_1(t, \mathbf{x}) = \begin{cases} \sin(2\pi t/T), & \mathbf{x} \in [0, H] \times [0, H], \\ 0, & \text{otherwise;} \end{cases}$$

$$f_2(t, \mathbf{x}) = \begin{cases} \cos(2\pi t/T), & \mathbf{x} \in [0, H] \times [0, H], \\ 0, & \text{otherwise.} \end{cases}$$

For the parameters in GMsFEM, we use “A+B” to denote that A local basis functions are used in each local domain in offline stage 1 while B bases are added for each local domain in offline stage 2. The dimension of snapshot space is 13481×1000 . In particular, 13481 is total number of fine-grid nodes while 1000 is the number of global snapshots bases in the global snapshot space. In terms of

whether time is contained in the inputs, we prepare two types of datasets (\mathcal{D}_1 and \mathcal{D}_2). The sizes for \mathcal{D}_1 and \mathcal{D}_2 are 1000 and 10000, respectively. More specifically, \mathcal{D}_1 contains 1000 sets of different KL terms, while \mathcal{D}_2 has 100 sets of KL terms. For each KL term in \mathcal{D}_2 , we choose 100 uniformly distributed time points $\{t_i\}$, where $t_i = \frac{i}{100}T$ for $i = 1, \dots, 100$. In a training process or a test process, a whole set \mathcal{D}_1 or \mathcal{D}_2 will be used. For a training process, we use k-fold cross-validation to divide \mathcal{D}_1 or \mathcal{D}_2 into a training set (S_{train}) and a validation set (S_{valid}). Adam [42] is used as the optimizer in training. We choose the learning rate to be 0.01 and batch size to be 50. We further define following loss:

$$\mathcal{L} = \sum_{i=1}^{N_{train}} \|\hat{p}_i - p_i\|_{L^2}, \quad (37)$$

where p_i and \hat{p}_i are defined to be a reference solution and a corresponding model prediction, respectively. Based on (37), the goal of a training process can be formulated as a optimization problem as (34). To estimate the performance, we define an error e by

$$e = \sum_{i=1}^N \frac{\|\hat{p}_i - p_i\|_{L^2}}{\|p_i\|_{L^2}} / N, \quad (38)$$

where N is the number of elements in the corresponding set.

5.2.1 Different structures of NN

In this subsection, we compare the performances of NNs with different depths and widths. In particular, we denote

- NN₁: A 2-layer NN with each hidden layer composed of 5 neurons;
- NN₂: A 3-layer NN with each hidden layer composed of 5 neurons;
- NN₃: A 4-layer NN with each hidden layer composed of 5 neurons;
- NN₄: A 2-layer NN with each hidden layer composed of 10 neurons;
- NN₅: A 2-layer NN with each hidden layer composed of 15 neurons.

The local multiscale basis number is chosen to be “2+3”. Inputs for time-independent NNs are 4 KL expansion coefficients and outputs are 40 POD coefficients at the final time. As for time-dependent NNs, inputs consist of KL expansion coefficients as well as a specific time $t \in [0, T]$. The outputs are corresponding coefficients with respect to POD bases at the particular time t . We note that the number of layers here is referred to the number of hidden layers in this paper.

	NN ₁	NN ₂	NN ₃
S_{train}	0.0922	0.0642	0.0673
S_{valid}	0.0925	0.0645	0.0675
S_{test}	0.0925	0.0645	0.0677

Table 3: Errors of the time-independent NNs with different depths on training, validation and test sets. 2-layer, 3-layer and 4-layer NNs with 5 neurons for each layer. Time is not included in inputs.

In Table 3 and Table 4, we display errors (defined in (38)) corresponding to time-independent and time-dependent networks with different depths. In particular, networks with 2,3,4 hidden layers are used in all three different sets (training, validation and test). There are two conclusions. Firstly, the network performs almost the same among three datasets. The validation error is higher than the training error but the test error is almost identical with the training error. This shows that

	NN ₁	NN ₂	NN ₃
S_{train}	0.0674	0.0704	0.0688
S_{valid}	0.0778	0.0816	0.0795
S_{test}	0.0696	0.0726	0.0710

Table 4: Errors of time-dependent NNs with different depths on training, validation and test sets. 2-layer, 3-layer and 4-layer NNs with 5 neurons for each layer. Time is included in inputs.

	NN ₁	NN ₄	NN ₅
S_{train}	0.0922	0.0663	0.0639
S_{valid}	0.0925	0.0663	0.0640
S_{test}	0.0925	0.0667	0.0643

Table 5: Errors of the time-independent NNs with different widths on training, validation and test sets. 2-layer NNs with 5,10, 15 neurons for each layer. Time is not included in inputs.

	NN ₁	NN ₄	NN ₅
S_{train}	0.0674	0.0668	0.0667
S_{valid}	0.0778	0.0766	0.0764
S_{test}	0.0696	0.0689	0.0688

Table 6: Errors of time-dependent NNs with different widths on training, validation and test sets. 2-layer NNs with 5,10, 15 neurons for each layer. Time is included in inputs.

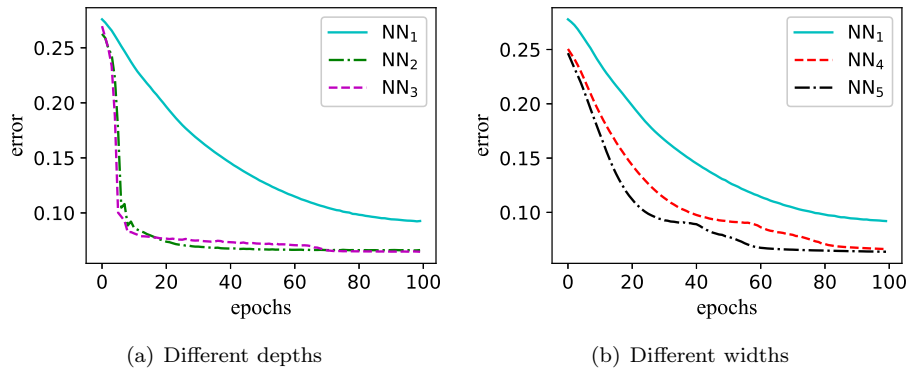


Figure 4: Error of time-independent NNs with different depths and widths in training process. (a): Loss curves of 2-layer, 3-layer, 4-layer NNs, with each layer composed of 5 neurons. (b) Loss curves of three 2-layer NNs, with 5, 10, 15 neurons for each layer.

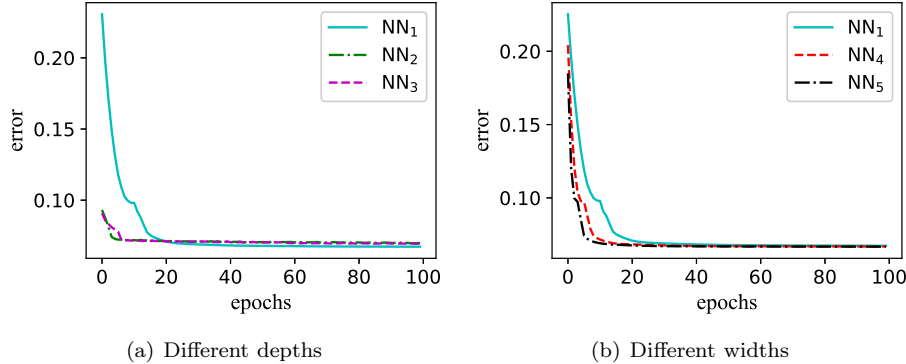


Figure 5: Error of time-dependent NNs with different depths and widths in training process. (a): Loss curves of 2-layer, 3-layer, 4-layer NNs, with each layer composed of 5 neurons. (b) Loss curves of three 2-layer NNs, with 5, 10, 15 neurons for each layer.

once trained, the neural network is good at generalization. For example, in the time-independent NN₁, the test error is 9.25% which is slightly larger than that of the training set (9.22%). Secondly, adding a single layer can remarkably decrease the error. When the number of layers is sufficient, no further error reduction will be attained by increasing the number of layers. As shown in Table 3, the test error of NN₂ (6.45%) is smaller than NN₁ (9.25%) and even smaller than NN₃ (6.77%). As for the time-dependent NNs (Table 3), the case is slightly different. The performance of NN₁ is best among three NNs in terms of the final accuracy after a training process. In particular, the test error of NN₁ is 6.96%, smaller than that of NN₂ (7.26%) and NN₃ (7.10%). From this, we can observe that the error reduction from adding layers is not guaranteed.

Results of networks with different widths, 5, 10, 15 neurons for each layer, are shown in Table 5 and 6, corresponding to the time-independent and time dependent NNs, respectively. From the Tables, we have two observations. Firstly, as width increases, higher accuracy is obtained. In Table 5, the test errors of NNs with 5, 10, 15 neurons in each layer are 9.25%, 6.89% and 6.43% respectively. Secondly, when time is added in the inputs, the performance of NNs are almost identical, which shows the proposed reduced deep learning method can be applied in a more generalized case.

In Figure 4 and Figure 5, error history in training a time-independent and a time-dependent NN are shown. In particular, results of 2-layer, 3-layer and 4-layer NNs are compared in subfigures 4(a) and 5(a), where each layer contains 5 neurons. In subfigures 4(b) and 5(b), error dynamics associated with 2-layer NNs with different widths (5, 10, 15 neurons for each layer) are presented. From subfigure 4(a), one can see that as the depth of NNs increases, the corresponding error converges faster. However, the final error of NN₂ is the smallest, which is the same as shown in Table 3. In subfigure 4(b), similar pattern can be recognized. More neurons in each layer will accelerate the error decay. Error in NN₅ decreases faster than that in NN₁ and NN₄. Besides, the error of NN₅ remains steady at a lowest level. In the time-dependent case, three curves of different NNs share high similarity. In Table 5(a) and 5(b), three curves are frozen almost simultaneously. More specifically, the NN₅ in Table 5(b) converges slightly faster than NN₁ and NN₄.

Overall, the 2-layer NN with 15 neurons in each layer can give the best estimations among the 5 alternatives in the sense of final accuracy and convergence rate of loss. Hence we will use the architecture of NN₅ in the rest experiments under the subsection 5.2.

5.2.2 Comparison of NN prediction with POD solution

To assess the effectiveness of the DL based approach, we compare the NN predictions with the corresponding POD solutions. We will test time-independent NNs and time-dependent NNs separately as follows. For the previous case, inputs are 4 KL expansion coefficients and outputs are 20 POD

coefficients. Since the time-independent NN produces POD coefficients associated to the final time, no specific time t is incorporated in the inputs. On the other hand, inputs of a time-dependent NN consist of 4 KL expansion coefficients and a particular time t , and NN produces 20 POD solutions at the time t . As before, we show results for three sets: training set, validation set and test set.

Final errors of time-independent and time-dependent NNs are displayed in Table 7 and Table 8. From the results, we can see that the NN approximations are better than the POD method for each set. In the time-independent case, the NN errors of training, validation and test sets are 9.53%, 9.54% and 9.55% while POD errors are 11.67%, 11.67% and 22.79% respectively. The differences are even larger in the time-dependent case. The training error of NN is 6.9% while the POD error in the same set is 12.28%, nearly twice as large as the NN error. The POD error in the test set (23.42%) is more than three times of the NN error (7.14%). Different sources are used in training and test sets. The relative bad performance of the POD approximation in a test set resulted from the application of POD bases which are generated with a different source used in a training set. However, NNs performs almost the same for the training set and test set, which shows that NN is better in generalization than previously developed POD method [38].

	S_{train}	S_{valid}	S_{test}
NN	0.0953	0.0954	0.0955
POD	0.1167	0.1167	0.2279

Table 7: Comparison of the errors between time-independent NNs and the GMsFEM-POD method for the linear flow problem (4). A 2-layer NN with 15 neurons on each layer is used.

	S_{train}	S_{valid}	S_{test}
NN	0.0690	0.0804	0.0714
POD	0.1228	0.1228	0.2342

Table 8: Comparison of the errors between time-dependent NNs and the GMsFEM-POD method for the linear flow problem (4). A 2-layer NN with 15 neurons on each layer is used.

5.2.3 Time-independent case

In this subsection, we consider the time-independent NNs, where the time is not included in the inputs. We will investigate the effect of following two factors:

1. Different dimensions of inputs layer and output layer;
2. Different numbers of multiscale bases.

We first study the influences from the numbers of KL expansion coefficients and POD coefficients, which represent the dimension of the input and output layers, respectively. More specifically, we consider following cases:

- 4 KL expansion coefficients, 20,30,40 POD coefficients;
- 15 KL expansion coefficients, 20,30,40 POD coefficients;
- 25 KL expansion coefficients, 20,30,40 POD coefficients.

In Tables 9-11, we show the final step errors associated with 4, 15, 25 KL expansion coefficients and 20, 30, 40 POD coefficients. We note that each column corresponds to one choice of a POD coefficients number. Three observations can be obtained. First of all, the error decays as more POD bases are used. For example, from Table 9, the training error decreases from 7.93% to 6.48% if the number of POD bases increases from 20 to 40. Similar phenomenons can be observed in

	20	30	40
S_{train}	0.0793	0.0714	0.0648
S_{valid}	0.0796	0.0716	0.0650
S_{test}	0.0797	0.0718	0.0651

Table 9: Final errors corresponding to the data associated with 4 KL expansion coefficients and 20, 30, 40 POD coefficients.

	20	30	40
S_{train}	0.0803	0.0736	0.0672
S_{valid}	0.0815	0.0748	0.0684
S_{test}	0.0808	0.07741	0.0677

Table 10: Final errors corresponding to data associated with 15 KL expansion coefficients and 20, 30, 40 POD coefficients.

	20	30	40
S_{train}	0.0814	0.0737	0.0686
S_{valid}	0.0835	0.0761	0.0724
S_{test}	0.0821	0.0744	0.0697

Table 11: Final errors corresponding to data associated with 25 KL expansion coefficients and 20, 30, 40 POD coefficients.

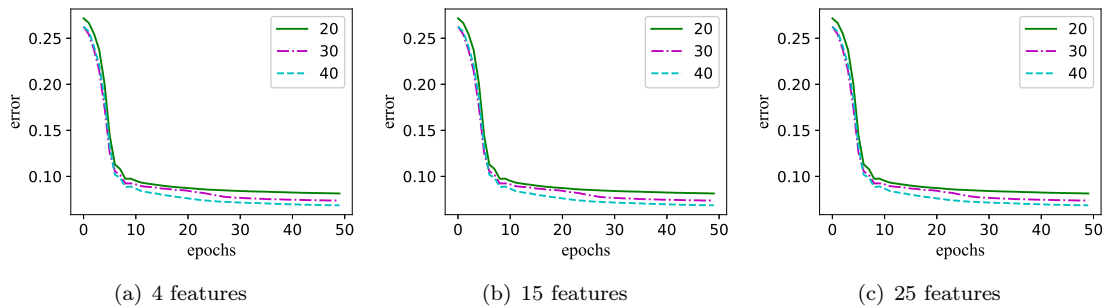


Figure 6: Comparison of error curves corresponding to different POD bases with the same number of features in the training process. 4, 15, 25 KL expansion coefficients are chosen. For each chosen of feature dimension, 20, 30, 40 POD bases are applied individually.

the cases that 15 and 25 KL expansion terms are used. Another observation is that if the number of POD bases is fixed, the error will increase as more KL expansion coefficients are input to the network. For example, with 40 POD bases, the testing error grows to 6.97% from 6.51% if the number of KL expansion coefficients increase from 4 to 25. Moreover, as more KL expansion coefficients are incorporated, the error gap between the training set and test set expands due to the increasing randomness. In other words, the difficulty in generalization increases as more features are considered.

We then explore the effect of the number of local multiscale bases. We choose 4 KL expansion coefficients as inputs and 40 POD coefficients as outputs and use NN_5 . Two basis combinations “2 + 3” and “8 + 0” are considered.

	S_{train}	S_{valid}	S_{test}
“2 + 3”	0.0654	0.0655	0.0657
“8 + 0”	0.0761	0.0764	0.0765

Table 12: Final errors corresponding to different combinations of multiscale bases. NN_1 is trained. Data contains 4 KL expansion coefficients and 40 POD bases.

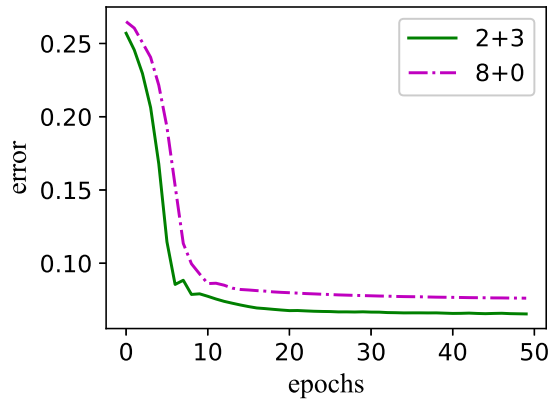


Figure 7: Comparison of the error corresponding to different multiscale bases in the training process. NN_1 is trained. Data contains 4 KL expansion coefficients and 40 POD bases.

In Table 12, we show the final errors associated with the cases of “2 + 3” and “8 + 0” are used. We can see the performance of “2 + 3” is better than “8 + 0”, which shows the efficiency of adding residual-driven bases in initial local basis space. In particular, in the “2 + 3” case, the training, validation and test errors are 6.54%, 6.55% and 6.57%, respectively, while the errors of “8 + 0” are 7.61%, 7.64% and 7.65%. The error history of these two cases are displayed in Figure 7. It can be observed that errors in both cases decrease rapidly and slow down after certain epochs. Even though there are small oscillations in the “2 + 3” case, the error decays faster than the “8 + 0” case. Besides, it is worth mentioning that after the error of “8 + 0” keeps steady, the error of the other case still has a tendency to decrease. The result in Figure 7 verifies the final error gap between these two cases shown in Table 12.

5.2.4 Time-dependent case

In this subsection, we consider time-dependent NNs, in which the time is also included in the input layer. We are also interested in how the dimension of the input and output layers and the number of multiscale bases influence the performance of NNs.

	20	30	40
S_{train}	0.0791	0.0749	0.0707
S_{valid}	0.0794	0.0751	0.0709
S_{test}	0.0794	0.0752	0.0710

Table 13: Errors corresponding to time-dependent data associated with 4 KL expansion coefficients and 20, 30, 40 POD coefficients.

	20	30	40
S_{train}	0.0811	0.0759	0.0720
S_{valid}	0.0816	0.0764	0.0723
S_{test}	0.0814	0.0763	0.0724

Table 14: Errors corresponding to time-dependent data associated with 15 KL expansion coefficients and 20, 30, 40 POD coefficients.

	20	30	40
S_{train}	0.0810	0.0811	0.0755
S_{valid}	0.0816	0.0818	0.0760
S_{test}	0.0814	0.0815	0.0759

Table 15: Errors corresponding to time-dependent data associated with 25 KL expansion coefficients and 20, 30, 40 POD coefficients.

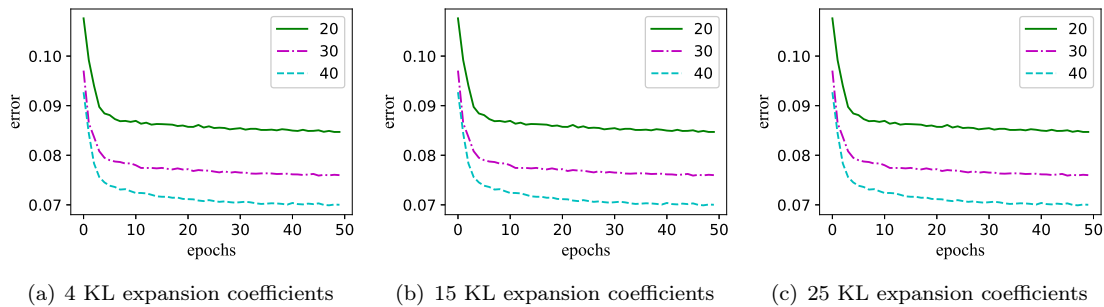


Figure 8: Comparison of the errors corresponding to different POD bases with the same number of features in the training process. 4, 15, 25 KL expansion coefficients are chosen. Time is input as a feature. For each chosen of feature dimension, 20, 30, 40 POD bases are applied individually.

In Table 13-15, we show the errors of time-dependent NNs corresponding to different numbers of POD coefficients where the numbers of KL expansion coefficients are 4, 15 and 25, respectively. Similar to the time-independent case, two observations are obtained. Firstly, higher accuracy is attained if more POD bases are incorporated. For example, the test errors in Table 14 are 8.14%, 7.63% and 7.24% associated with 20, 30 and 40 POD bases, respectively. Moreover, the error increases with more KL expansion coefficients incorporated due to the fact that higher dimensionality of input will bring more complexity of the NN. In Figure 8, curves of training error in the training process are displayed. In particular, we compare errors associated with different POD coefficients in subfigures 8(a), 8(b) and 8(c), corresponding to 4, 15, 25 KL expansion coefficients respectively. The comparisons displayed in these three figures share obvious similarity. As more POD bases are used, the error decays faster and it levels off at an earlier point.

	S_{train}	S_{valid}	S_{test}
“2 + 3”	0.0705	0.0817	0.0729
“8 + 0”	0.0814	0.0929	0.0838

Table 16: Errors corresponding to different combinations of multiscale bases. NN_5 is trained. Data contains 4 KL expansion coefficients and 40 POD bases. Time is included in the data features.

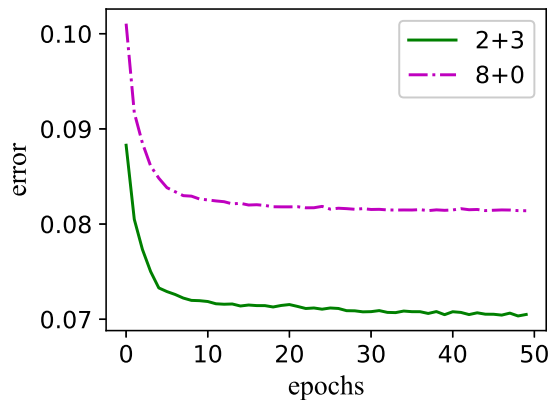


Figure 9: Comparison of the errors corresponding to different multiscale bases in the training process. NN_1 is trained. Data contains 4 KL expansion coefficients and 40 POD bases. Time is included in the data features.

Finally, we show how multiscale bases numbers influence the performance of the time-dependent NNs. In Table 16, “2 + 3” and “8 + 0” cases are compared using three datasets. Similar to the time-independent case, the “2 + 3” case can yield more accurate solutions than the “8 + 0” case. In particular, the training, validation and test errors of “2 + 3” are 7.05%, 8.17% and 7.29% compared with 8.14%, 9.29% and 8.38% in the “8 + 0” case. In Figure 9, we show the comparison of the error history, we can see the error curve representing “2 + 3” decays faster and tends steady at a lower level. In a word, residual driven basis is more efficient in approximations.

5.3 Nonlinear flow

In this subsection, we apply our method to the following nonlinear flow problem.

$$\begin{cases} \frac{\partial p}{\partial t} - \operatorname{div}(\kappa(\mathbf{x}; \omega, p) \nabla p) = f(t, \mathbf{x}), & (t, \mathbf{x}, \omega) \in (0, T) \times \Omega \times \Omega_r, \\ p(t, \mathbf{x}) = 0, & (t, \mathbf{x}) \in (0, T) \times \partial\Omega, \\ p(0, \mathbf{x}) = g(\mathbf{x}), & (t, \mathbf{x}) \in \{t = 0\} \times \Omega. \end{cases} \quad (39)$$

Here $\kappa(\mathbf{x}; \omega, p)$ depends on p . Explicitly, $\kappa(\mathbf{x}; \omega, p) = \kappa(\mathbf{x}; \omega) \rho_r \exp(c(p - p_r))$, where ρ_r, p_r, c are some given constants and $\kappa(\mathbf{x}; \omega)$ is the random variable present in (3).

We use different source terms $f_3(\mathbf{x})$ and $f_4(\mathbf{x})$ for training and test stage, respectively.

$$f_3(\mathbf{x}) = \begin{cases} 1/2, & \mathbf{x} \in \zeta_i, i = 1, \dots, 4, \\ -3, & \mathbf{x} \in \zeta_5, \\ 0, & \text{otherwise}; \end{cases}$$

$$f_4(\mathbf{x}) = \begin{cases} 1/2, & \mathbf{x} \in \zeta_i, i = 1, 2, \\ -3, & \mathbf{x} \in \zeta_5, \\ 0, & \text{otherwise}, \end{cases}$$

where $\zeta_i, i = 1, \dots, 4$ are fine elements at the four corners of Ω . In particular, $\zeta_1 = [0, h] \times [0, h]$, $\zeta_2 = [L_x - h, L_x] \times [0, h]$, $\zeta_3 = [0, h] \times [L_y - h, L_y]$, $\zeta_4 = [L_x - h, L_x] \times [L_y - h, L_y]$. Moreover ζ_5 is the fine element at the center of Ω . More specifically, $\zeta_5 = [\lfloor \frac{L_x}{2h} \rfloor h, (\lfloor \frac{L_x}{2h} \rfloor + 1)h] \times [\lfloor \frac{L_y}{2h} \rfloor h, (\lfloor \frac{L_y}{2h} \rfloor + 1)h]$.

In the following two subsections, the multiscale basis number is chosen to be “4+1”. Inputs for time-independent NNs are 4 KL expansion coefficients and outputs are 40 POD coefficients at the final time. For time-dependent NNs, a specific time $t \in (0, T]$ is included in the inputs of time-dependent NNs and the outputs are associated to the input t .

5.3.1 Different structures of NN

In this subsection, we compare the performances of NNs with different width and depths for the nonlinear problem. More specifically, we explore following architectures:

- NN₁: A 2-layer NN with each hidden layer composed of 10 neurons;
- NN₂: A 3-layer NN with each hidden layer composed of 10 neurons;
- NN₃: A 4-layer NN with each hidden layer composed of 10 neurons;
- NN₄: A 2-layer NN with each hidden layer composed of 20 neurons;
- NN₅: A 2-layer NN with each hidden layer composed of 30 neurons.

	NN ₁	NN ₂	NN ₃
S_{train}	0.0954	0.0281	0.0255
S_{valid}	0.0953	0.0280	0.0256
S_{test}	0.0942	0.0273	0.0242

Table 17: Errors of the time-independent NNs with different depths on training, validation and test sets. 2-layer, 3-layer and 4-layer NNs with 10 neurons for each layer. Time is not included in inputs.

	NN ₁	NN ₄	NN ₅
S_{train}	0.0954	0.0506	0.0159
S_{valid}	0.0953	0.0504	0.0161
S_{test}	0.0942	0.0503	0.0189

Table 18: Errors of the time-independent NNs with different widths on training, validation and test sets. 2-layer NNs with 10, 20, 30 neurons for each layer. Time is not included in inputs.

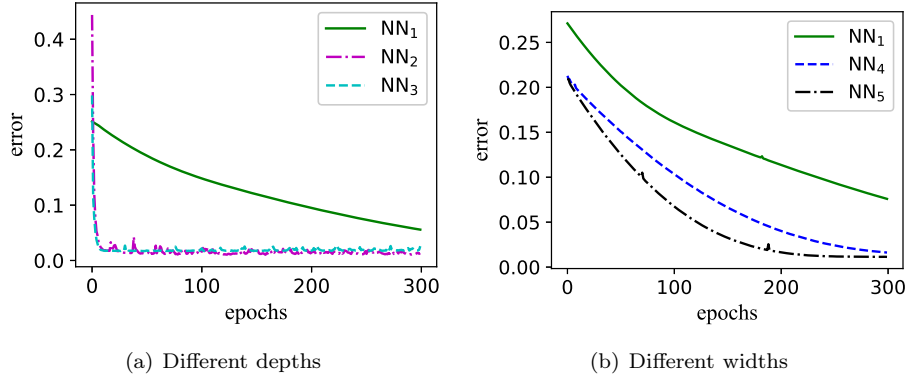


Figure 10: Errors of the time-independent NNs with different depths and widths in training process. (a): Loss curves of 2-layer, 3-layer, 4-layer NNs, with each layer composed of 10 neurons. (b) Loss curves of three 2-layer NNs, with 10, 20, 30 neurons for each layer.

In Table 17, we compare three NNs (2, 3, 4 hidden layers) with 10 neurons in each layer. The shown results are average error of 1000 set of samples. We denote three NNs by NN₁, NN₂ and NN₃. We observe that if more layers are used, the final error will decrease. In particular, training error, validation error and test error with NN₁ are 9.54%, 9.53% and 9.42%. With NN₂ and NN₃, the errors are all about 2%. Hence, only one layer will tremendously increase accuracy. Figure 10(a) shows that using more hidden layers will dramatically increase the convergence of error. In Table 18, NNs of same depth and different widths are estimated. Here, we consider 2-layer NNs with 10, 20 and 30 neurons for each layer. As more neurons are used, the errors decline gradually. In particular, the training errors of NN₁, NN₄ and NN₅ are 9.54%, 5.06% and 1.59%, respectively. From Figure 10(b), we can see that with wider NNs one can obtain faster convergence rate.

5.3.2 Comparison of NN prediction and POD solution

We compare the neural network predictions with POD solutions in this subsection. k-fold cross-validation is applied to generate training set and validation set. We note that the GMsFEM with Newton's method [24] is applied to solve snapshots associated with (39).

Similar to the linear case, we construct both the time-independent and time-dependent NNs. In the time independent case, we use 1000 sets of parameters for both training set \mathcal{D}_1 and test set \mathcal{D}_2 . As for the time-dependent case, we use 100 sets of parameters and 10 uniform distributed time steps for each choice of parameter.

In Table 19, we show the mean errors of the time-independent NN predictions and POD solutions. The time in the input layer is set to be the final time T . We can see the NN errors are less than twice of the POD errors. Since the POD errors are all less than 1%, the NN predictions are relatively low. For instance, the NN errors for training set, validation set and test sets are 1.59%, 1.60% and 1.88%, respectively.

We compare the time-dependent NN prediction with POD solutions in Table 20. The NN errors are about three times of the corresponding POD errors, but all errors are small. Similar to the time-independent case, since the POD solutions are quite accurate, the NN errors are also very small. For example, the POD error and the NN error for training set are 0.8% and 1.54%. At the same time, NN evaluation is much faster than POD approximation. Once the NN is trained, the testing time is almost negligible. However, in the POD approach, it requires several Newton iterations in each time step, which is time-consuming. CPU time elapsed in a single online valuation with these two methods are shown in Table 21. The NN evaluation is about 10^5 times faster than the POD approach, which shows the high performance of reduced NN method.

	S_{train}	S_{valid}	S_{test}
NN	0.0159	0.0160	0.0188
POD	0.0094	0.0094	0.0096

Table 19: Comparison of the error between time-independent NNs and the GMsFEM-POD method for the nonlinear flow problem (39). 2-layer NN with 30 neurons on each layer is used.

	S_{train}	S_{valid}	S_{test}
NN	0.0154	0.0165	0.0148
POD	0.0080	0.0080	0.0081

Table 20: Comparison of the error between time-dependent NNs and the GMsFEM-POD method for the nonlinear flow problem (39). 2-layer NN with 30 neurons on each layer is used.

	NN	POD
CPU Time	4×10^{-5}	1.2

Table 21: CPU time comparison for each single online evaluation with the NN and POD method.

6 Conclusion

A deep learning based reduced-order method is proposed in this article. GMsFEM-POD are developed for generating the data for training the neural network in the offline stage, rigorous analysis of the GMsFEM-POD is presented, which provides as a milestone for the neural-network approach. Once a network is well-trained, online computation is fast owing to the reduced-order architecture. Two kinds of networks are proposed, depending on whether time is incorporated in the input of the neural network. Through non-trivial groundwater problems, the performance of the proposed neural network has been compared with previous GMsFEM-POD, demonstrating that the neural-network approach is better in efficiency and generalization. In particular, we consider linear and nonlinear stochastic flow problems. In the linear case, using different source terms in training test and test set, the NN predictions are much more accurate than POD predictions, especially in the test sets. As for the nonlinear case, NN predictions have slightly larger errors compared with POD solutions. But since POD solutions are sufficiently accurate, the NN errors are relatively low. Furthermore, the CPU time in online stage is significantly reduced with the deep learning approach since Newton iterations are needed in POD approximations. Besides, among five tested neural network architectures, the network consisting of two hidden layers provides best approximations. Hence a very shallow network is sufficient in this context. Furthermore, influence of utilizing different numbers of KL expansion coefficients, POD coefficients and multiscale bases are studied, providing a reference for further research and practical applications. Future work includes the applications for this method for more complicated flow problems such as compressible two phase flow.

Acknowledgement

The research of Eric Chung is partially supported by the Hong Kong RGC General Research Fund (Project numbers 14304719 and 14302620) and CUHK Faculty of Science Direct Grant 2020-21.

References

- [1] Todd Arbogast, Gergina Pencheva, Mary F Wheeler, and Ivan Yotov. A multiscale mortar mixed finite element method. *Multiscale Modeling & Simulation*, 6(1):319–346, 2007.

- [2] Maxime Barrault, Yvon Maday, Ngoc Cuong Nguyen, and Anthony T Patera. An ‘empirical interpolation’ method: application to efficient reduced-basis discretization of partial differential equations. *Comptes Rendus Mathematique*, 339(9):667–672, 2004.
- [3] Saifon Chaturantabut and Danny C Sorensen. Nonlinear model reduction via discrete empirical interpolation. *SIAM Journal on Scientific Computing*, 32(5):2737–2764, 2010.
- [4] Peng Chen, Alfio Quarteroni, and Gianluigi Rozza. Comparison between reduced basis and stochastic collocation methods for elliptic problems. *Journal of Scientific Computing*, 59(1):187–216, 2014.
- [5] Yan Chen and Dongxiao Zhang. Data assimilation for transient flow in geologic formations via ensemble kalman filter. *Advances in Water Resources*, 29(8):1107–1122, 2006.
- [6] Zhiming Chen and Thomas Hou. A mixed multiscale finite element method for elliptic problems with oscillating coefficients. *Mathematics of Computation*, 72(242):541–576, 2003.
- [7] Kenny Choo, Antonio Mezzacapo, and Giuseppe Carleo. Fermionic neural-network states for ab-initio electronic structure. *Nature communications*, 11(1):1–7, 2020.
- [8] Michael Andrew Christie and MJ Blunt. Tenth spe comparative solution project: A comparison of upscaling techniques. *SPE Reservoir Evaluation & Engineering*, 4(04):308–317, 2001.
- [9] E. T. Chung, Y. Efendiev, and T. Leung. Residual-driven online generalized multiscale finite element methods. *Journal of Computational Physics*, 302:176–190, 2015.
- [10] Eric Chung, Yalchin Efendiev, and Thomas Y Hou. Adaptive multiscale model reduction with generalized multiscale finite element methods. *Journal of Computational Physics*, 320:69–95, 2016.
- [11] Eric T Chung and Yalchin Efendiev. Reduced-contrast approximations for high-contrast multiscale flow problems. *Multiscale Modeling & Simulation*, 8(4):1128–1153, 2010.
- [12] Davide Cortinovis and Patrick Jenny. Iterative Galerkin-enriched multiscale finite-volume method. *Journal of Computational Physics*, 277:248–267, 2014.
- [13] L. J. Durfolsky. Numerical calculation of equivalent grid block permeability tensors of heterogeneous porous media: Water resour res v27, n5, may 1991, p299–708. In *International Journal of Rock Mechanics and Mining Sciences & Geomechanics Abstracts*, volume 28, page A350. Pergamon, 1991.
- [14] Y. Efendiev and T. Y. Hou. *Multiscale finite element methods: theory and applications*, volume 4. Springer Science & Business Media, 2009.
- [15] Keinosuke Fukunaga and Warren LG Koontz. Application of the Karhunen-Loeve expansion to feature selection and ordering. *IEEE Transactions on computers*, 100(4):311–318, 1970.
- [16] Benjamin Ganis, Ivan Yotov, and Ming Zhong. A stochastic mortar mixed finite element method for flow in porous media with multiple rock types. *SIAM Journal on Scientific Computing*, 33(3):1439–1474, 2011.
- [17] Mengwu Guo and Jan S Hesthaven. Data-driven reduced order modeling for time-dependent problems. *Computer methods in applied mechanics and engineering*, 345:75–99, 2019.
- [18] Jiequn Han, Linfeng Zhang, and E Weinan. Solving many-electron schrödinger equation using deep neural networks. *Journal of Computational Physics*, 399:108929, 2019.

- [19] Jan Hermann, Zeno Schätzle, and Frank Noé. Deep-neural-network solution of the electronic schrödinger equation. *Nature Chemistry*, 12(10):891–897, 2020.
- [20] Jan S Hesthaven, Gianluigi Rozza, Benjamin Stamm, et al. *Certified reduced basis methods for parametrized partial differential equations*, volume 590. Springer, 2016.
- [21] Jan S Hesthaven and Stefano Ubbiali. Non-intrusive reduced order modeling of nonlinear problems using neural networks. *Journal of Computational Physics*, 363:55–78, 2018.
- [22] Thomas Y Hou and Xiao-Hui Wu. A multiscale finite element method for elliptic problems in composite materials and porous media. *Journal of computational physics*, 134(1):169–189, 1997.
- [23] Thomas JR Hughes, Gonzalo R Feijóo, Luca Mazzei, and Jean-Baptiste Quinicy. The variational multiscale method—a paradigm for computational mechanics. *Computer methods in applied mechanics and engineering*, 166(1-2):3–24, 1998.
- [24] Carl T Kelley. *Solving nonlinear equations with Newton’s method*. SIAM, 2003.
- [25] YC Liang, HP Lee, SP Lim, WZ Lin, KH Lee, and CG Wu. Proper orthogonal decomposition and its applications—part i: Theory. *Journal of Sound and vibration*, 252(3):527–544, 2002.
- [26] Ivan Lunati and Patrick Jenny. Multi-scale finite-volume method for highly heterogeneous porous media with shale layers. In *ECMOR IX-9th European Conference on the Mathematics of Oil Recovery*, pages cp–9. European Association of Geoscientists & Engineers, 2004.
- [27] Warren S McCulloch and Walter Pitts. A logical calculus of the ideas immanent in nervous activity. *The bulletin of mathematical biophysics*, 5(4):115–133, 1943.
- [28] Federico Negri, Andrea Manzoni, and David Amsallem. Efficient model reduction of parametrized systems by matrix discrete empirical interpolation. *Journal of Computational Physics*, 303:431–454, 2015.
- [29] David Pfau, James S Spencer, Alexander GDG Matthews, and W Matthew C Foulkes. Ab initio solution of the many-electron schrödinger equation with deep neural networks. *Physical Review Research*, 2(3):033429, 2020.
- [30] KK Phoon, HW Huang, and ST Quek. Simulation of strongly non-Gaussian processes using karhunen–loève expansion. *Probabilistic engineering mechanics*, 20(2):188–198, 2005.
- [31] Alfio Quarteroni, Andrea Manzoni, and Federico Negri. *Reduced basis methods for partial differential equations: an introduction*, volume 92. Springer, 2015.
- [32] Gianluigi Rozza, Dinh Bao Phuong Huynh, and Anthony T Patera. Reduced basis approximation and a posteriori error estimation for affinely parametrized elliptic coercive partial differential equations. *Archives of Computational Methods in Engineering*, 15(3):229–275, 2008.
- [33] Danny Smyl and Dong Liu. Less is often more: Applied inverse problems using hp-forward models. *Journal of Computational Physics*, 399:108949, 2019.
- [34] Shiliang Sun, Zehui Cao, Han Zhu, and Jing Zhao. A survey of optimization methods from a machine learning perspective. *IEEE transactions on cybernetics*, 50(8):3668–3681, 2019.
- [35] Maria Vasilyeva, Masoud Babaei, Eric T Chung, and Denis Spiridonov. Multiscale modeling of heat and mass transfer in fractured media for enhanced geothermal systems applications. *Applied Mathematical Modelling*, 67:159–178, 2019.

- [36] Maria Vasilyeva, Eric T Chung, Yalchin Efendiev, and Jihoon Kim. Constrained energy minimization based upscaling for coupled flow and mechanics. *Journal of Computational Physics*, 376:660–674, 2019.
- [37] Karen Veroy, Christophe Prud’Homme, Dimitrios Rovas, and Anthony Patera. A posteriori error bounds for reduced-basis approximation of parametrized noncoercive and nonlinear elliptic partial differential equations. In *16th AIAA Computational Fluid Dynamics Conference*, page 3847, 2003.
- [38] Yiran Wang, Eric Chung, and Shubin Fu. A local-global generalized multiscale finite element method for highly heterogeneous stochastic groundwater flow problems. *arXiv preprint arXiv:2105.05413*, 2021.
- [39] Yiran Wang, Eric Chung, Shubin Fu, and Zhaoqin Huang. A comparison of mixed multiscale finite element methods for multiphase transport in highly heterogeneous media. *Water Resources Research*, 57(5):e2020WR028877, 2021.
- [40] Mary Fanett Wheeler, Guangri Xue, and Ivan Yotov. A multiscale mortar multipoint flux mixed finite element method. *ESAIM: Mathematical Modelling and Numerical Analysis-Modélisation Mathématique et Analyse Numérique*, 46(4):759–796, 2012.
- [41] X. Wu, Y. Efendiev, and T. Y. Hou. Analysis of upscaling absolute permeability. *Discrete and Continuous Dynamical Systems Series B*, 2(2):185–204, 2002.
- [42] Zijun Zhang. Improved adam optimizer for deep neural networks. In *2018 IEEE/ACM 26th International Symposium on Quality of Service (IWQoS)*, pages 1–2. IEEE, 2018.